Topics in Catalysis (2020) 63:1754–1764
https://doi.org/10.1007/s11244-020-01304-0

ORIGINAL PAPER

On the Promoting Effects of Te and Nb in the Activity and Selectivity of M1 MoV-Oxides for Ethane Oxidative Dehydrogenation

Daniel Melzer[1] · Gerhard Mestl[2] · Klaus Wanninger[2] · Andreas Jentys[1] · Maricruz Sanchez-Sanchez[1] · Johannes A. Lercher[1,3]

Published online: 8 July 2020

Abstract
The pathways of ethane oxidative dehydrogenation and total combustion have been elucidated for M1 phase type Mo–V oxide catalysts with different metal composition. The ethane oxidation mechanism is not affected by the presence of Te or Nb. Conversely, the selectivity is strongly affected by stoichiometry of M1 catalysts. This is attributed to the facile oxidation of ethene to CO_x upon formation of unselective VO_x species in the absence of Te and Nb.

Keywords Ethane ODH · Mo-V oxide catalysts · M1 phase · Selective oxidation

1 Introduction

Oxidative dehydrogenation (ODH) of ethane is an alternative route for the production of ethene. The process can be operated already at moderate temperatures (300–400 °C) in contrast to steam cracking of ethane and is economically feasible at small scale [1]. $MoVTeNbO_x$ mixed metal oxide catalysts were found to be highly active and selective for the dehydrogenation of ethane [1]. These mixed metal oxides contain mostly two crystalline phases [2]; i.e., the orthorhombic M1 phase and the pseudo-hexagonal M2 phase. The M1 phase (ICSD pattern no. 55097) of mixed Mo-V oxides has been recognized one of the most active and selective catalysts for ethane ODH [3–5].The M1 phase is able to activate alkanes by initial abstraction of a hydrogen atom [7]. Its catalytic activity was found to linearly correlate with the V^{5+} surface concentration [8]. This led to the generally accepted conclusion, that similar to other vanadium oxidation catalyst, vanadyl $\{V^{5+}{=}O \leftrightarrow V^{4+}{-}O\bullet\}$ surface species are responsible for hydrogen abstraction [9]. Among the different possible formulations of the M1 phase, the Mo–V–Te–Nb mixed oxide has been identified as an excellent catalyst for the oxidative dehydrogenation of ethane [10]. However, the positive effect of Te and Nb is not understood at a level to derive guidance for improved syntheses.

The M1 phase exhibits an orthorhombic crystal structure, with the basal {001} plane formed by edge and corner sharing distorted metal–oxygen octahedra (Fig. 1). Repetitive stacking of the unit cell structure in the (001) direction results in hexagonal and heptagonal channels parallel to this direction. Crystallographic sites S1 to S11 are occupied by Mo and/or V. Nb prefers the pentagonal crystal site S9 and Te–O units partially occupy six- and seven-membered ring positions (S12 and S13 respectively) [11, 12].

It has been shown that the M1 structure allows for some chemical flexibility with respect to the nature and oxidation state of site occupancies [12–14]. The catalytic activity has been attributed to $V^{5+}{=}O$ species located in the crystallographic sites S2-S4-S7 [8, 11, 15, 16] and, therefore, higher V contents in the crystalline M1 structure have been concluded to increase the probability of a unit cell containing an active site.

Electronic supplementary material The online version of this article (https://doi.org/10.1007/s11244-020-01304-0) contains supplementary material, which is available to authorized users.

✉ Maricruz Sanchez-Sanchez
m.sanchez@tum.de

✉ Johannes A. Lercher
Johannes.lercher@ch.tum.de

[1] Department Chemie & Catalysis Research Center, TU München, Lichtenbergstr. 4, 85747 Garching, Germany

[2] Clariant Produkte (Deutschland) GmbH, Waldheimer Str. 13, 83502 Bruckmühl, Germany

[3] Institute for Integrated Catalysis, Pacific Northwest National Laboratory, Richland WA 99,352, USA

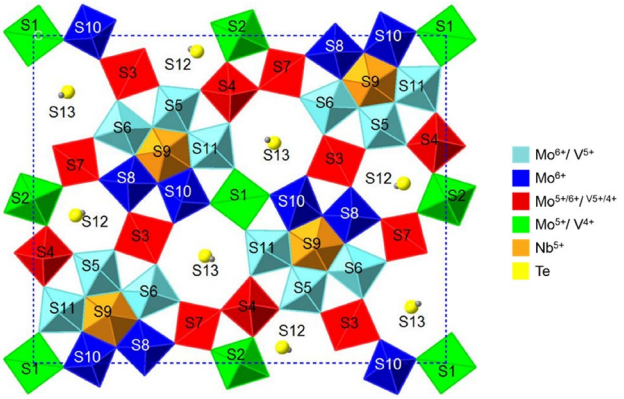

Fig. 1 Representation of M1 phase viewed along the c-axis direction with 13 cation sites as published in [6]. Different colors of polyhedral indicate the suggested occupancy of crystallographic sites by different metals and oxidation states as labelled

The role of reducible Te–O units adjacent to the active sites of M1 has been subject of vivid debates for these materials. It has been proposed that Te–O increases activity by enhancing alkane adsorption [17], aiding reoxidation of V^{4+} spent species [18], or participating in the abstraction of first H from the alkane [19]. In situ studies combined with theory have pointed to electronic effects due to the reduction of Te sites as origin of additional catalytic activity [20].

Here, we study the role of the metal composition of M1 catalysts on the product distribution, activity and selectivity in oxidative dehydrogenation of ethane. Recently, we developed a new synthesis method that enables the preparation of phase pure M1 MoV(Te,Nb)O_x with significantly higher surface and intrinsically higher density of active sites [21]. Using this method, we have prepared a series of high surface area M1 materials with identical V content but different Te and Nb concentrations. Detailed kinetic tests of ethane and ethene oxidation are combined with bulk and surface physico-chemical characterization of MoV(TeNb)O_x with the aim of correlating elemental composition to catalytic performance in ethane ODH.

2 Experimental

Synthesis of MoV(TeNb)O_x materials was performed as described in a prior contribution [21]. In brief, MoO_3, V_2O_5, TeO_2, $Nb_2O_5{\cdot}1.5H_2O$, citric acid (CA), oxalic acid (OA) and mono ethylene glycol (EG) were dispersed in millipore grade H_2O. The concentration of Mo was fixed at 0.5 mol/l and rest of the metal concentrations were varied accordingly to the nominal stoichiometry targeted. The additives molar ratio relative to Mo was Mo:CA:EG = 1:0.075:0.075, with OA varying with Nb content with a ratio Nb:OA of 1. Hydrothermal synthesis was performed in a Premex Reactor AG hpm-p stainless steel autoclave at 190 °C and 17.5 bar(a) for 48 h. All crude precipitated materials were dried in static air at 80 °C for 16 h after hydrothermal synthesis. Preconditioning of the materials to reaction temperatures was performed at 400 °C in flowing N_2 for 2 h, with a heating ramp of 15 °C/min.

X-ray diffraction analysis were performed on a PANalytical Empyrian or PANalytical X'pert Pro diffractometers in a Bragg–Brentano geometry (θ- 2θ-goniometer), using copper-Kα radiation and operating at 45 kV and 40 mA. The scanning range was 5°–70° 2θ with increments of 0.017°. For the quantification of the amorphous content, the metal oxide sample was thoroughly mixed with about 10 wt.-% of a fully crystalline Rutile (r-TiO_2) standard material obtained from NIST. Diffractogram and Rietveld analysis was performed using PANalytical Highscore Plus v3 software. Quantification of the amorphous content was done according to the procedure described elsewhere [6]. Surface areas were determined by N_2 adsorption at − 196 °C using a Sorptomatic 1990 automated surface area and pore size analyzer. Prior to the measurements all samples were evacuated at a temperature of 250 °C and a pressure of 10^{-2} mbar for 2 h. Surface area was calculated according to the Brunnauer-Emmett-Teller (BET) method and pore volumes and pore size distribution were calculated using the Barrett-Joyner-Halenda (BJH) model. Error of the measurement is < 1%. Elemental analysis was performed on an Agilent 760 ICP-OES spectrometer. Metal concentrations were determined using 281.615 nm (Mo), 311.817 nm (V), 214.282 nm (Te) and 313.178 nm (Nb) emission lines. Solid mixed metal oxide samples were fused in soda-potash mixture before being dissolved in millipore grade water. The morphology of M1 phase particles was characterized using a high-resolution scanning electron microscope 7500F ColdFEG (JEOL) operating at an accelerating voltage of 2.0 kV and emission current of 10 µA. Working distance was about 8 mm.

The X-ray photoelectron (XPS) measurements were performed by Physical Electronics GmbH, Ismaning, Germany. The XPS spectra were obtained in a PHI Quantum 2000 spectrometer equipped with a 180° hemispherical electron analyzer and a Al-Kα ($h\nu = 1486.68$ eV) X-ray source powered at 100 W. Prior the measurements the powder samples were evacuated at 25 °C for 2 h. The base pressure in the ion pumped analysis chamber was maintained at $5{\bullet}10^{-7}$ Pa during data acquisition. Experimental spectra were fitted by a least-squares routine supplied by the instrument manufacturer using Gaussian and Lorentzian lines, after smoothing and substraction of the S-shaped background. Peak intensities were used to calculate atomic ratios via normalization with atomic sensitivity factors from NIST X-ray photoelectron spectroscopy database. The binding energies were referenced to the value of C 1 s peak from carbon contamination at 284.6 eV. The inelastic mean free path (IMFP), and hence

information depth of the photoelectrons, was calculated using the algorithm by Penn et al. [22]. The IMFP is 1.8 nm (V) and 2.4 nm (Mo) using MoO_3 as model compound for M1, in accordance with Heine et al. [23]. These lengths are in the range of one M1 unit cell measured along the *a* or *b* axes and five unit cells along the *c* axis.

X-ray absorption spectra were recorded at the V K-edge on beamline P65 at PETRA III (DESY) in Hamburg, Germany. The electron energy was 6 GeV with a beam current of 100 mA. The beam size at the sample was 200 × 300 µm. Around 10 mg of the sample was sandwiched between quartz wools and packed in a quartz capillary reactor (1 mm outer diameter, 0.02 mm wall thickness), and placed on top of a gas-blower for controlled heating. A double-crystal Si(111) monochromator was used to control the incident photon energy and the spectra were recorded with ionization chamber detectors in a transmission mode. Linear combination fits of V K-edge XANES spectra were done using $VOSO_4$ and V_2O_5 measured spectra as V^{4+} and V^{5+} references respectively.

Catalyst performance was tested in a glass-lined, stainless-steel tubular reactor with an inner diameter of 4 mm. Catalytic activity was tested in a lab scale fixed bed plug flow reactor at atmospheric pressure in the temperature range of 330–420 °C. The catalyst material was pressed and sieved to a size range of 150–212 µm and diluted with SiC (mass ratio: 1:5) of the same particle size. Prior to reaction the catalysts were treated 400 °C in flowing N_2 for 2 h, with a heating ramp of 15 °C/min. The reaction gas feed was 50 ml/min of 9.1 mol-% ethane, 9.1 mol-% O_2 and 81.8 mol-% inert. Weight hourly space velocity (WHSV) is calculated as follow:

$$WHSV = \frac{F_{Total} * x_{Ethane} * \rho_{Ethane}}{m_{cat}}$$

Reactor entry and exit are equipped with silica wool plugs. In front of the catalyst bed 200 mg of SiC ensured an axially homogeneous heat distribution. Feed and product gas was analyzed using a Shimadzu GC2014 gas chromatography system equipped with TCD and FID detector capable of quantifying C_2-hydrocarbons and -oxygenates, CO and CO_2, O_2 and N_2. The latter was used as internal standard to ensure closure of the carbon balance within ± 2%.

3 Results

3.1 Effects of Te and Nb Content on ODH Activity and Selectivity of High Surface M1-MoV(TeNb)O_x

The series of M1-phase catalysts with nominal compositions $MoV_{0.30}Te_{0–0.10}Nb_{0–0.10}O_x$ was prepared as part of the optimization of a new synthetic method for high surface area M1 materials [21]. In this work, we aim to investigate the influence of metal composition on the selectivity in ethane ODH for high surface area M1-phase catalysts.

Table 1 Physico-chemical properties of as-prepared (dried overnight at 80 °C) $MoV_{0.30}Te_{0–0.10}Nb_{0–0.10}O_x$ materials, as reported in reference [21]

ICP-OES formula	BET (m^2/g)	M1 wt.-%	Amorphous / wt.-%	Other phases
$MoV_{0.30}O_X$	97	N.d.[a]	N.d.[a]	N.d.[a]
$MoV_{0.30}Te_{0.05}Nb_{0.05}O_X$	59	77	22	None
$MoV_{0.31}Te_{0.05}Nb_{0.10}O_X$	71	58	40	NbO_2
$MoV_{0.31}Te_{0.12}Nb_{0.08}O_X$	74	52	47	Te^0
$MoV_{0.30}Te_{0.10}Nb_{0.09}O_X$	87	59	40	Te^0

[a]Rietveld refinement was not possible due to missing long range order

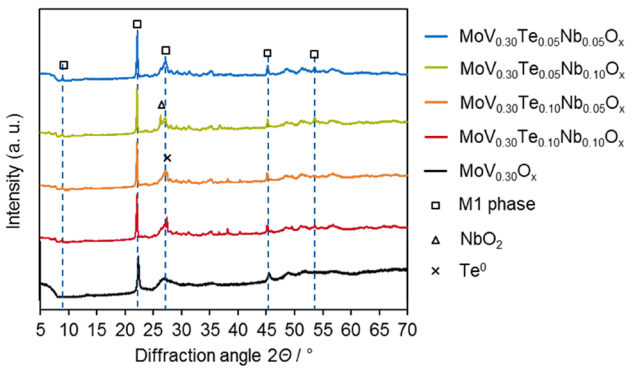

Fig. 2 X-ray diffractograms of as-prepared $MoV_{0.30}Te_{0-0.10}Nb_{0-0.10}O_x$ mixed oxides, as reported in reference [21]

Table 1 shows the physico-chemical properties of the catalysts as prepared, i.e., dried at 80 °C overnight after hydrothermal synthesis. The bulk elemental composition of the samples agrees well with the nominal compositions (i.e., the ratio of metals used in hydrothermal synthesis). X-ray diffraction analysis showed that the materials are mostly crystallized M1 phase, with 20–50% of amorphous material being present. Broadening of the diffraction peaks is frequently observed in this type of materials and it is attributed to the presence of short range ordered domains with M1 structure [21, 24, 25]. Therefore, it should be noted that the quantification of catalytically active M1 from the XRD data underestimates the real concentrations of this phase. In the case of the high surface Mo-V binary sample the broadening of M1 diffraction peaks does not allow for a Rietveld analysis and quantification of M1 content (Fig. 2). On the

other hand, presence of other crystalline phases can be ruled out for all the samples, and only trace concentrations below 2 wt.% (MoO_3, NbO_2 or metallic Te) were detected in some cases.

Prior to catalysis, the materials, synthesized below 200 °C, were heated up to reaction temperatures in N_2. To ensure thermal stability, the catalyst was kept at 400 °C for 1 h in N_2 admitting the ODH mixture and the catalysts were analyzed with respect to crystallinity—as quantified by XRD—and surface area of the M1 phase materials. As it can be seen in Table S1 crystallinity was not significantly affected. Specific surface areas were observed to decrease by 15% in Te and Nb containing samples (from 59 to 50 m^2/g) and up to 35% for MoV only M1 (from 97 to 63 m^2/g).

Catalytic tests detected clear variations in ethane ODH activity and selectivity within the investigated range of M1 phase metal compositions. Figure 3 shows the ethene production rates, normalized to the catalyst masses, obtained over five different samples. The presence of small concentrations of Te (Te/Mo = 0.05, blue hollow symbols) results in the highest ODH rates. The Nb/Mo ratio did not affect the ODH rates within the tested range of stoichiometries.

The apparent energies of activation obtained for ethene formation were identical, i.e., 76 ± 2.0 kJ mol^{-1}, for all tested catalysts. Therefore, we conclude that differences in the rates are caused only by differences in the pre-exponential factors or the concentration of active sites. This indicates that the reaction mechanism of ODH-E is not affected by the chemical composition of M1 nanocrystals within the tested range, but that metal stoichiometry influences the rate constants or concentration of active sites.

The chemical composition, however, affected the selectivity to ethene. Figure 4 shows the selectivities to ethene (A), CO (B) and CO_2 (C) as a function of ethane conversion for the catalysts shown in Fig. 3. Those catalysts with Te/Mo ratios lower or equal to Nb/Mo ratios (blue) had the highest

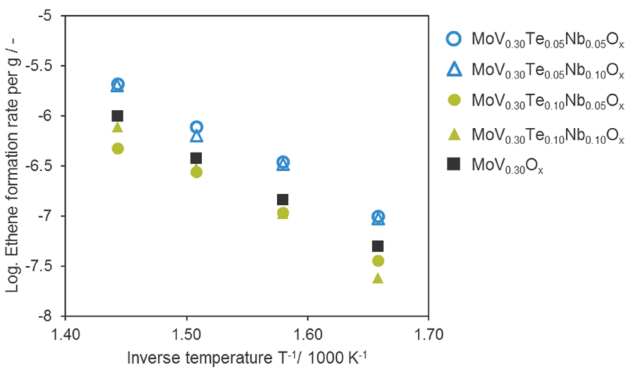

Fig. 3 Arrhenius plots of the catalytic tests of materials with various $MoV(TeNb)O_x$ formulations in the ethane ODH. Reactions conditions applied: T = 330–420 °C, C_2H_6:O_2:inert = 9:9:82, p = 1 bar(a), $WHSV$ = 20 h^{-1}

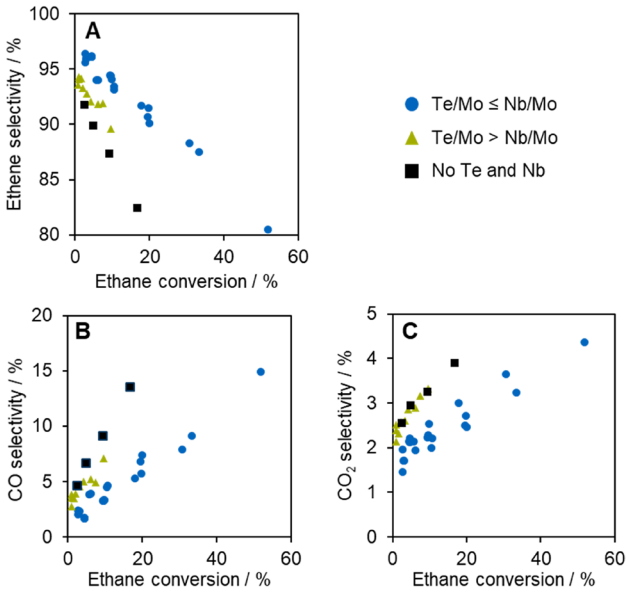

Fig. 4 Ethene (**a**), CO (**b**) and CO_2 (**c**) selectivities for various $MoV(TeNb)O_x$ formulations in ODH-E. Reactions conditions applied: T = 330–420 °C, C_2H_6:O_2:inert = 9:9:82, p = 1.0 bar(a) (B-M1), $WHSV$ = 3.6–17.4 h^{-1}

ethene selectivity up to conversion levels of about 50%. In contrast, the catalyst in which Te/Mo was larger than Nb/Mo (green) and the one without any Te and Nb (black) showed relatively high selectivities to CO and CO_2. The differences were most significant at high conversions.

In order to study the origin of the effect of Te and Nb on the activity and selectivity, we selected two samples for further kinetic and physico-chemical characterization: quaternary $MoV_{0.30}Te_{0.05}Nb_{0.05}O_x$ ("Q-M1" in the following) showing high activity and selectivity to ethene, and binary $MoV_{0.30}O_x$ ("B-M1" in the following) showing comparably poor activity and selectivity in ethane ODH.

3.2 Physicochemical Properties of Quaternary and Binary M1 Catalysts

Figure 5 shows scanning electron micrographs of quaternary (Q-) and binary (B-) M1 metal oxides. Q-M1 crystallizes as bundles of rod-like particles, which is characteristic for the anisotropic growth along the *c*-axis of M1 crystals [26]. The B-M1 particles also have the principal morphology of the M1 phase, but the length of the rods is smaller and with a lower aspect ratio. We speculate that these particles are highly defective or have only small M1 domains in agreement with the higher degree of disorder of B-M1 observed by XRD.

Chemical composition of surface layers as well as the corresponding oxidation states of metal cations were derived from X-ray photoelectron spectra. The inelastic mean free

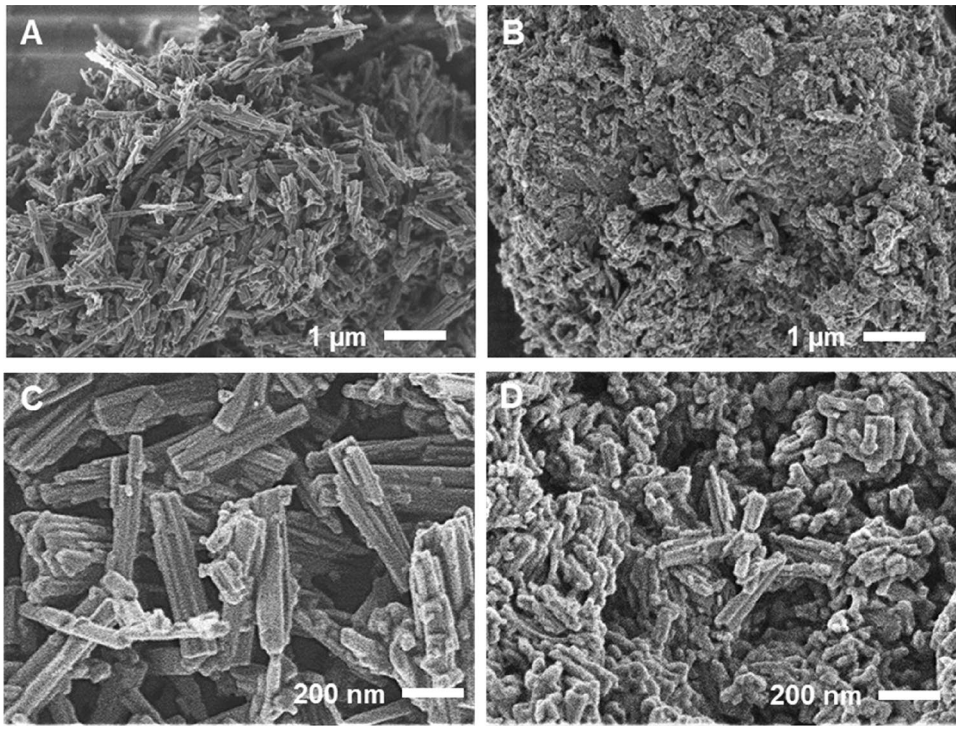

Fig. 5 SEM images at different magnifications of Q-M1 ($MoV_{0.30}Te_{0.05}Nb_{0.05}O_x$, panels **a** and **c**) and B-M1 ($MoV_{0.30}O_x$, panels **b** and **d**) samples

path (IMFP), and hence information depth of the photoelectrons is in the range of one M1 unit cell measured along the *a* or *b* axes and five unit cells along the *c* axis. Experimental spectra and peak deconvolution are shown in Figure S1. Surface concentrations of metal species calculated from XPS intensities and their corresponding oxidation states are compiled in Table 2.

Although there is a small shift to lower electron binding energies of Mo $3d_{5/2}$ electrons in the Q-M1 sample compared to B-M1, binding energies values of close to 233 eV in M1 [27, 28] and molybdenum oxides [29, 30] are attributed to Mo^{6+}. Binding energies of Te $3d_{5/2}$ (576.7 eV) and Nb $3d_{5/2}$ (207.3 eV) core levels in Q-M1 are attributed to Te^{4+} [31, 32] and Nb^{5+} [33, 34] oxidation states. V $2p_{3/2}$ spectra typically shows two contributions with binding energies at 516.6 eV and 517.6 eV, attributed to V^{4+} and V^{5+}, respectively [28, 31, 35, 36]. Interestingly, the surface V^{4+}/V^{5+} ratio as calculated from XPS is close to unity in B-M1, while about four times more V^{4+} than V^{5+} was observed in the layers near the surface of Q-M1. High V^{4+} surface concentrations have been reported before in XPS measurements for M1, indicating that likely the majority of V species on the lattice surface are V^{4+} state, while the bulk preserves the expected mixed oxidation state for V in M1 [28]. Thus, the high surface concentration of V^{5+} in B-M1 sample needs further examination.

While partial occupation of hexagonal channel sites (S12 in Fig. 1) with Te in M1-$MoVTeNbO_x$ is well-known [37], recent STEM [38] and single crystal XRD [39] studies proposed that those sites in M1-$MoVO_x$ can be partially

Table 2 Surface metal concentrations of $MoVTeNbO_x$ and $MoVO_x$ samples as determined by XPS

Orbital	Binding energy/eV	Assignment	Q-M1 Concentration (brackets: rel. to Mo)/at.-%	B-M1 Concentration (brackets: rel. to Mo)/at.-%
Mo $3d_{5/2}$	232.9 (Q-M1)	Mo^{6+}	23 (1.0)	24 (1.0)
	233.0 (B-M1)			
V $2p_{3/2}$	517.6	V^{5+}	0.59 (0.02)	1.9 (0.08)
	516.6	V^{4+}	1.8 (0.08)	2.4 (0.09)
Te $3d_{5/2}$	576.7	Te^{4+}	1.0 (0.04)	0
Nb $3d_{5/2}$	207.3	Nb^{5+}	0.23 (0.01)	0
O 1s	530.8	M-O_x	64 (2.8)	66 (2.8)
	532.0	M-OH	8.2 (0.35)	6.6 (0.28)

occupied by V^{5+} cations. Therefore, the higher XPS V^{5+}/Mo ratio found for a high surface area MoV-M1 here is tentatively attributed to the contribution to surface composition of V^{5+} units at the opening of hexagonal channels.

X-ray absorption spectroscopy was used to analyze the V oxidation state in the bulk of the oxides. Although the fitting of experimental spectra to a linear combination of reference spectra V_2O_5 and $VOSO_4$ references did not satisfactorily match all the pre-edge and edge features (Figure S2), the analysis allows concluding that both Q- and B-M1 samples have a similar estimated V oxidation state of 4.4 (ca. 60% V^{4+} and 40% V^{5+}). Thus, it can be concluded that the bulk oxidation state of V in M1 samples with similar V/Mo ratios is not affected by the presence of Te and Nb in the concentrations studied here. The surface oxidation state, however, is dramatically affected.

3.3 Kinetic Investigations of the Ethane Reaction Pathway

Having established the metal composition and oxidation states in the surface region of M1 particles, we now aim to gain further insight into the kinetics of the ethane oxidation. Figure 6 shows the selectivities to ethene, carbon oxides and acetic acid as a function of ethane conversion obtained over Q-M1 and B-M1 catalysts.

Ethene is the preferred reaction product over the whole conversion range tested, although selectivity is generally lower on B-M1 than on Q-M1. At ethane conversion levels above 5%, B-M1 displays a CO selectivity significantly higher than Q-M1. However, the selectivities extrapolated to zero conversion are similar for both M1 catalysts, with only about 2–3% higher CO selectivity at expenses of ethene on the B-M1 catalyst.

The selectivity to CO in the 0–20% conversion range increases in both B-M1 and Q-M1 at the expense of ethene and, in a lesser extent, acetic acid.

Further analysis by the Delplot analysis method [40, 41] clarifies the origin of the different byproducts in ethane ODH. The rank of product formation, i.e., primary vs. higher rank products, was established by first and second rank Delplots. The first rank Delplot is equivalent to the selectivity vs. conversion representation as shown in Fig. 6. It clearly shows that C_2H_4 is a primary product, while the rest of the products cannot be clearly classified by extrapolation to X = 0. Therefore, a second rank Delplot is necessary, where primary products appear as curves diverging near 0 conversion. This is clearly the case for acetic acid (Fig. 7) and C_2H_4 (not shown for clarity) on both B-M1 and Q-M1 catalysts. In the case of CO and CO_2, trends also bend at low conversions, although extrapolation would lead to a finite Y axis intercept. This is characteristic of a stable primary and secondary product and implies that a fraction of CO and CO_2 is formed via direct pathways from ethane, without desorption of any gaseous intermediates. Direct formation of CO_x from alkanes has been also reported in kinetic studies over other Mo-V oxidation catalysts [42].

The apparent activation energies obtained for ethene formation over Q-M1 and B-M1 shows that this pathway has the lowest barrier, ca. 76 ± 1.2 kJ mol^{-1}, followed by CO_2 (91 ± 3.4 kJ mol^{-1}) and CO formation (120 ± 6.0 kJ mol^{-1}). Figure S3 shows Arrhenius type plots of the formation rates of ethene, CO_x and acetic acid in the range of 330–420 °C. Due to bending lines in the Arrhenius plot of acetic acid formation, it was not possible to derive the activation energy. The different activation energies for each of the main reaction products ethene, CO and CO_2 imply that the rate determining steps are different for each of the three products, but similar over both catalysts. Virtually parallel lines in the Arrhenius plots in Figure S3 indicate that the two catalysts studied have identical apparent activation energies for each of the reaction pathways of ethane oxidation. This indicates that the MoV-backbone of M1 structure is responsible for activation of ethane and that the effect of metal composition in catalytic performance is only related to the number of active sites that are existing on M1 surfaces.

At differential conversions, all products are formed with a higher rate on Q-M1 compared to B-M1. This observation

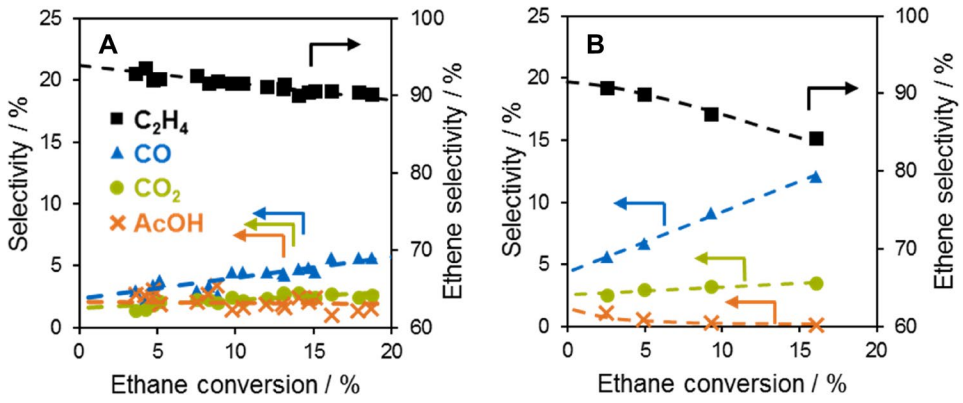

Fig. 6 Ethane oxidation product selectivities obtained over Q-M1 (**a**) and B-M1 (**b**). Reactions conditions applied: T = 290–370 °C (Q-M1), 330–420 °C (B-M1); C_2H_6:O_2:inert = 3-9:3-9:82-94 (Q-M1), C_2H_6:O_2:inert = 9:9:82 (B-M1); p = 1.5–4.0 bar(a) (Q-M1), 1.0 bar(a) (B-M1); $WHSV$ = 4.8–19.0 h^{-1} (Q-M1), 4.8 h^{-1} (B-M1)

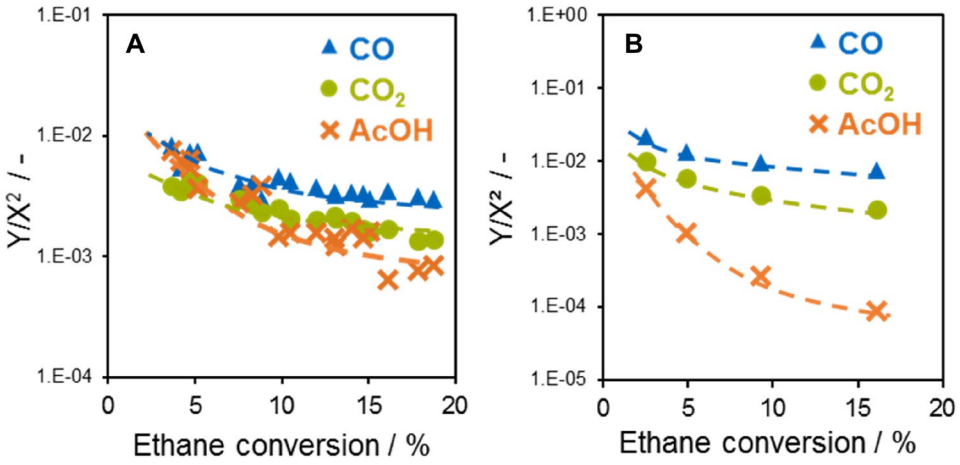

Fig. 7 Second rank delplots for ethane oxidation over Q-M1 (**a**) and B-M1 (**b**) samples. Reactions conditions applied: T = 290–370 °C (Q-M1), 330–420 °C (B-M1); C_2H_6:O_2:inert = 3-9:3-9:82-94 (Q-M1), C_2H_6:O_2:inert = 9:9:82 (B-M1); p = 1.5–4.0 bar(a) (Q-M1), 1.0 bar(a) (B-M1); $WHSV$ = 4.8–19.0 h^{-1} (Q-M1), 4.8 h^{-1} (B-M1)

holds also true for rates normalized to surface area as determined by N_2 adsorption (Figure S4), since both samples have BET values in the same order of magnitude. On the other hand, it should be noted that alkane oxidation activity is associated to V^{5+} species [8] and, therefore, the lower rates over B-M1, in spite of its higher V^{5+}/Mo fraction, needs further examination. We speculate that a large fraction of surface V^{5+} in B-M1 is not associated to structurally active surface positions but to VO_x inside 6-MR and/or 7-MR channels [38, 39], although formation of XRD-amorphous VO_x impurities cannot be ruled out.

3.4 Kinetics of Ethene Oxidation

In order to understand the differences in selectivity observed at ethane conversions above 5% for M1 catalysts with and without Te and Nb components, we studied the kinetics of ethene oxidation on B-M1 and Q-M1 samples. Figure 8 shows selectivities as a function of ethene conversion. Carbon oxides and acetic acid were the only observed products. Positive Y-axis intercepts indicate that carbon oxides and acetic acid are formed via direct reaction pathways. Over both catalysts, CO is the main reaction product. Constant selectivities of 80% CO and 18–20% CO_2 (with up to 2% selectivity to acetic acid) were observed for both catalysts when conversion levels exceeded 5% for Q-M1 and ca. 20% for B-M1. At low conversion levels, however, significant differences between both catalysts exist. The initial selectivity to CO is ca. 65% for both catalysts, but selectivity to acetic acid is significantly higher in the B-M1 that with Q-M1, indicating that, acetic acid tends to be decarboxylated on Q-M1. In any case, the high selectivity to CO in comparison to CO_2 from ethene oxidation further points to a direct CO_x formation route, because acetic acid oxidation is expected to produce equal amounts of CO and CO_2 [43].

Figure 9 shows that ethene oxidation rates are similar over both catalysts in the temperature range of 330–420 °C. However, contrary to ethane oxidation, there are pronounced differences in overall ethene oxidation barriers over Q- and B-M1 catalysts. Apparent E_A is 40 kJ mol^{-1} lower on B-M1 than on Q-M1 (Table 3). Similar energies of activation for the formation of CO and CO_2 on each catalyst indicate that these products likely have the same rate determining step,

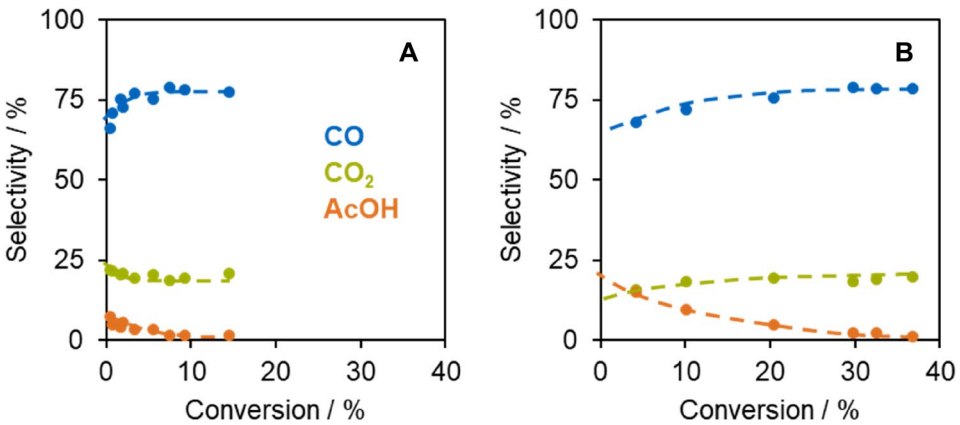

Fig. 8 Ethene oxidation product selectivities obtained over Q-M1 (**a**) and B-M1 (**b**). Reactions conditions applied: T = 330–420 °C (Q-M1 and B-M1); C_2H_6:O_2:inert = 3-9:3-9:82-94 (Q-M1), C_2H_6:O_2:inert = 9:9:82 (B-M1); p = 2.7–4.0 bar(a) (Q-M1 and B-M1); $WHSV$ = 16.9–19.3 h^{-1} (Q-M1), 4.8 h^{-1} (B-M1)

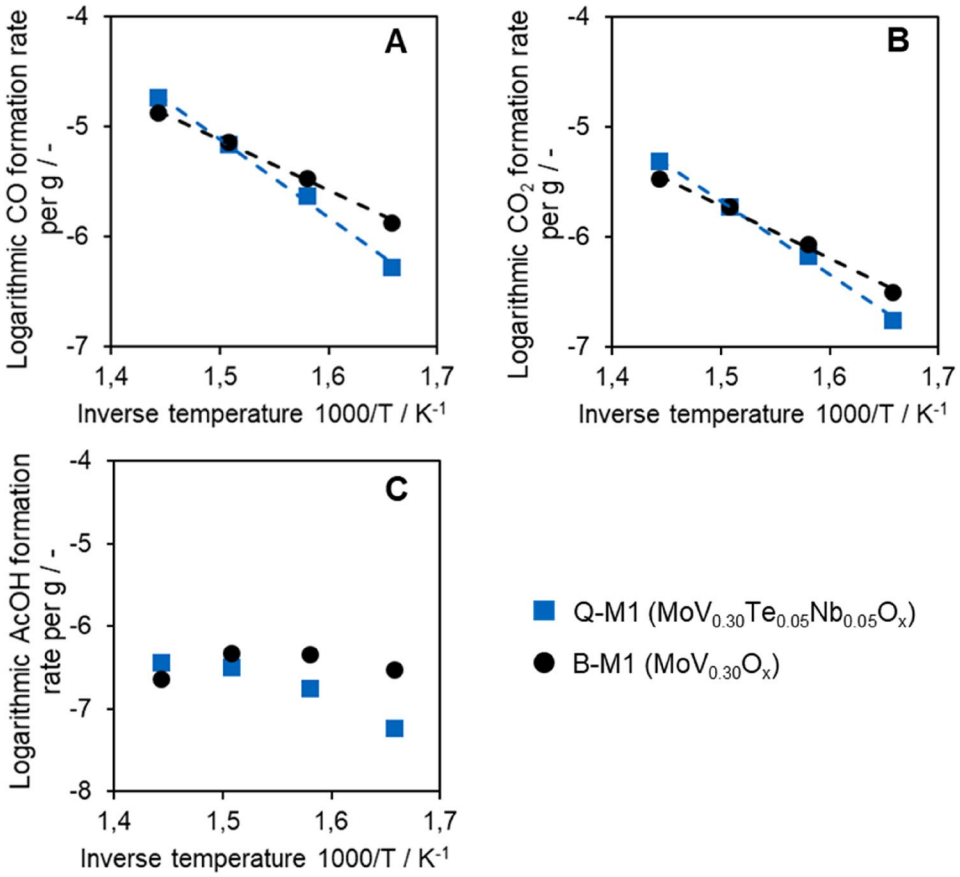

Fig. 9 CO (**a**), CO_2 (**b**) and acetic acid (**c**) formation rates in ethene oxidation over Q-M1 (blue squares) and B-M1 (black circles) normalized to weight of catalyst. T = 330–420 °C, C_2H_6:O_2:inert = 9:9:82, p = 4 bar(a), $WHSV$ = 17.1 h^{-1} (Q-M1), 4.8 h^{-1} (B-M1)

Table 3 Apparent activation energies E_A and corresponding standard deviation for all product formation pathways from ethane and ethene

Product	Reactant			
	Q-M1		B-M1	
	Ethane	Ethene	Ethane	Ethene
Ethene	78 ± 1.2	N/A	74 ± 0.19	N/A
CO	120 ± 5.4	140 ± 5.6	120 ± 2.7	100 ± 1.6
CO_2	89 ± 2.7	130 ± 3.6	93 ± 2.1	100 ± 3.1
AcOH	~ 0	~ 0	~ 0	~ 0
Overall	80 ± 1.4	135 ± 5.0	78 ± 0.7	92 ± 1.6

Values are given in kJ mol^{-1}

i.e., ethene activation. The apparent activation energy for acetic acid is zero, suggesting that its activation energy of formation equals its activation energy of decomposition.

4 Discussion

The similar activation energies on a series of high surface M1 materials with different Te and Nb contents (Fig. 3) allow us to conclude that active sites for ethane ODH are part of the M1 phase structure that does not directly involve

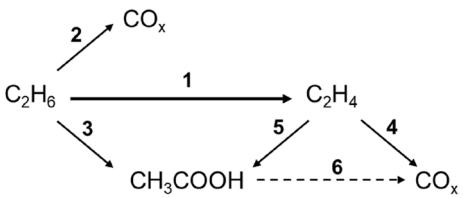

Scheme 1 Reaction pathways of ethane oxidation over M1 catalysts

Te and Nb. Catalysts containing small concentrations of Te (0.05 Te/Mo molar ratio) are more active than the other tested compositions, in spite of their similar V content and specific surface area. The fact that the reaction rates do not increase monotonically with Te content points to a promoting effect rather than adsorption enhancement exerted by this specific element. Thus, the higher activity of low-Te catalysts is concluded to be associated with a higher active site density. Conceptually, this can be caused by (i) the creation of additional oxygen radical sites in the material by partial Te reduction under reaction conditions [44] and/or (ii) a higher concentration of V^{5+} located in active surface lattice positions of the M1 framework.

Comparison of the kinetics of ethane and ethene oxidation shows that there are direct pathways for the formation of

CO and CO_2 both from C_2H_6 and C_2H_4. Based on the results of our study, the reaction pathways for ethane oxidation on M1 catalysts can be drawn as in Scheme 1.

The activation energies for the ethane total oxidation pathway are not affected by the presence of Te and Nb for ethane (routes 2 and 3 + 6 in Scheme 1), but they are ca. 40 kJ/mol different for ethene total oxidation (routes 4 and 5 + 6 in Scheme 1). The higher activation energy of ethene oxidation for catalysts containing Te and Nb agrees well with their higher ODH selectivity.

The selectivity towards CO_2 in ethane oxidation is similar on both binary and quaternary catalysts and does not vary significantly with conversion. Thus, we conclude that the formation of most of the CO_2 takes place by a pathway that does not involve the ethene intermediate and it likely stems from acetic acid oxidation (route 3 + 6 in Scheme 1). Conversely, the high CO/CO_2 ratio in ethane and ethene oxidation suggests that CO is mainly formed by pathways 2 and 4.

Apparent energies of activation in Table 3 show that formation of CO_2 has a barrier somewhat lower than CO formation. If we assume that CO_2 formation E_{app} in ethane oxidation (ca. 90 kJ/mol for both Q- and B-M1 catalysts, Table 3) represents the acetic acid decomposition via route 3 + 6, it can be concluded that Mo-V-only related M1 sites are catalyzing this reaction. Conversely, the ethene oxidation rate determining step is the activation of ethene and thus the CO and CO_2 formation barriers are both reflecting that value, regardless of a 4 or a 5 + 6 route of formation. In this scenario, the higher selectivity to acetic acid on B-M1 for ethene oxidation (Fig. 8) can be attributed to a lower proportion of Mo-V M1-sites catalyzing route 6 in comparison to VO_x-related unselective sites catalyzing 4 and 5.

Summarizing, the results show that ethane activation is intrinsically associated to Mo and V metal sites in the M1 structure. Oxidation of the acetic acid intermediate is also hypothesized to be independent from Te and Nb content. However, the reactivity of the ODH product C_2H_4, is affected by the presence of both metals, leading to differences in selectivities, especially at medium and high conversions.

ODH activity of M1 phase is commonly ascribed to oxygen radical sites located in the pentameric ensemble of crystallographic sites S2-S4-S7 in Fig. 1 [8, 11, 15, 16]. These sites can be occupied by Mo or V in different oxidation states in different proportions. Metal occupancy of M1 is affected by the synthesis method and by the oxide chemical composition, including the presence of other metals [20, 45]. B-M1 and Q-M1 share the same synthesis method and V/Mo ratio, so the statistical distribution of S2-S4-S7 metal occupancies could be regarded as similar. However, the oxidation state of V might differ in the two materials due to differences in the overall charge distribution in the lattice due to the presence of reducible Te units, as well as by the substitution of Mo by Nb in S9 sites. In the "active/inactive" scenario of Mo and V occupancies proposed by Grasselli [9], such differences would translate into changes in the overall concentration of available active sites, explaining differences in rates.

On the other hand, we have observed that the concentration of unselective sites catalyzing the oxidation of C_2H_4 to CO_x is affected by the presence of Te and Nb in M1catalysts. The synthesis of a highly disordered MoV-M1 catalyst generated a larger fraction of sites with a low barrier for ethene oxidation, thus leading to poor selectivity in the overall ethane ODH reaction over this catalyst.

The nature of the species responsible for the direct oxidation of ethene is not clear. Apparent energies of activation obtained for C_2H_4 oxidation on B-M1 (Table 3) are in the range of those described for supported vanadium oxides [46]. By XPS we have detected a high surface concentration of V^{5+} species in B-M1 that is not associated to alkane activation at the reaction temperatures used here. However, given the broad XRD peaks of B-M1 nanocrystalline sample, it is not possible to determine unambiguously whether the facile C_2H_4 oxidation is linked to VO_x impurities present on XRD-amorphous synthesis debris or to specific features of a binary M1 oxide (for instance, VO_x units in the pore mouth of 6- or 7-MR).

Thus, the higher ODH activity achieved by high surface M1 samples with Te/Mo and Nb/Mo ratios of 0.05 (Fig. 3) is attributed to a larger fraction of active sites, induced by the overall composition of the M1 lattice and, possibly, electronic effects of reducible Te species in the vicinity of the active sites [44]. The absence or very low concentration of unselective sites able to oxidize C_2H_4 results in a high ODH selectivity, and it is suggested to be linked to an optimized incorporation of V in the M1 lattice. This can be achieved by fine-tuning the synthesis parameters, including the presence of certain amounts of Te, Nb, and potentially other promoters, that direct V to occupy active positions and modulate its oxidation state.

5 Conclusions

The presence of Te and Nb in M1-type catalysts affects reaction rates as well as product distribution in oxidative dehydrogenation of ethane. Kinetic analysis of ethane and ethane oxidation pathways have shown that the reaction mechanism of ODH-E is not affected by the chemical composition of M1 nanocrystals within the tested range, but stoichiometry influences the concentration of active sites. The high olefin selectivity of $MoVTeNbO_x$ compared to $MoVO_x$ M1 is the consequence of higher energetic barriers for ethene oxidation in presence of Te and Nb. Tuning the $MoVTeNbO_x$ metal stoichiometry serves to adjust the Mo and V metal occupancy and oxidation state in the M1 lattice. In this way,

the formation of VO_x unselective sites responsible for the facile oxidation of ethene is minimized.

Acknowledgements Open Access funding provided by Projekt DEAL. This work was supported by the Bavarian Ministry of Economic Affairs, Energy and Technology (project number: 47-3665 g/1075/1-NW-1501-0003) and Clariant Produkte (Deutschland) GmbH. A.J. acknowledges the support of the BMBF within the Project MatDynamics (Verbundprojekt 05K13WO3). We acknowledge DESY (Hamburg, Germany), a member of the Helmholtz Association HGF, for the provision of experimental facilities. Parts of this research was carried out at PETRA III and we would like to thank Edmund Welter for assistance in using beamline P 65. Philipp Donaubauer is acknowledged for his helpful suggestions regarding Delplot analysis. Insu Lee is acknowledged for his help with XANES analysis.

Compliance with Ethical Standards

Conflict of interest The authors declare that they have no conflict of interest.

References

1. Cavani F, Ballarini N, Cericola A (2007) Oxidative dehydrogenation of ethane and propane: how far from commercial implementation? Catal Today 127:113–131
2. Ushikubo T, Oshima K, Kayou A, Hatano M (1997) Ammoxidation of propane over Mo-V-Nb-Te mixed oxide catalysts. In: Li C, Xin Q (eds) Studies in surface science and catalysis. Elsevier, Amsterdam, pp 473–480
3. Nieto JML (2006) The selective oxidative activation of light alkanes. From supported vanadia to multicomponent bulk V-containing catalysts. Topics Catal 41:3–15
4. Gärtner CA, van Veen AC, Lercher JA (2013) Oxidative dehydrogenation of ethane: common principles and mechanistic aspects. ChemCatChem 5:3196–3217
5. Grant JT, Venegas JM, McDermott WP, Hermans I (2018) Aerobic oxidations of light alkanes over solid metal oxide catalysts. Chem Rev 118:2769–2815
6. Melzer D, Xu P, Hartmann D, Zhu Y, Browning ND, Sanchez-Sanchez M, Lercher JA (2016) Atomic-scale determination of active facets on the MoVTeNb Oxide M1 Phase and their intrinsic catalytic activity for ethane oxidative dehydrogenation. Angew Chem Int Ed 55:8873–8877
7. Botella P, García-González E, López Nieto JM, González-Calbet JM (2005) MoVTeNbO multifunctional catalysts: correlation between constituent crystalline phases and catalytic performance. Solid State Sci 7:507–519
8. Naraschewski FN, Jentys A, Lercher JA (2011) On the role of the vanadium distribution in MoVTeNbO x mixed oxides for the selective catalytic oxidation of propane. Top Catal 54:639–649
9. Grasselli RK, Buttrey DJ, DeSanto P, Burrington JD, Lugmair CG, Volpe AF, Weingand T (2004) Active centers in Mo–V–Nb–Te–Ox (amm)oxidation catalysts. Catal Today 91–92:251–258
10. Botella P, Dejoz A, Abello MC, Vázquez MI, Arrúa L, López Nieto JM (2009) Selective oxidation of ethane: developing an orthorhombic phase in Mo–V–X (X=Nb, Sb, Te) mixed oxides. Catal Today 142:272–277
11. Grasselli RK, Buttrey DJ, Burrington JD, Andersson A, Holmberg J, Ueda W, Kubo J, Lugmair CG, Volpe AF (2006) Active centers, catalytic behavior, symbiosis and redox properties of MoV(Nb, Ta)TeO ammoxidation catalysts. Top Catal 38:7–16
12. DeSanto P, Buttrey DJ, Grasselli RK, Lugmair CG, Volpe AF, Toby BH, Vogt T (2004) Structural aspects of the M1 and M2 phases in MoVNbTeO propane ammomidation catalysts. Zeitschrift Fur Kristallographie 219:152–165
13. DeSanto P, Buttrey DJ, Grasselli RK, Lugmair CG, Volpe AF, Toby BH, Vogt T (2003) Structural characterization of the orthorhombic phase M1 in MoVNbTeO propane ammoxidation catalyst. Top Catal 23:23–38
14. Li X, Buttrey DJ, Blom DA, Vogt T (2011) Improvement of the structural model for the M1 Phase Mo–V–Nb–Te–O Propane (Amm)oxidation catalyst. Top Catal 54:614–626
15. Grasselli RK, Volpe AF (2014) Catalytic Consequences of a revised distribution of key elements at the active centers of the M1 phase of the MoVNbTeOx system. Top Catal 57:1124–1137
16. Schlögl R (2011) Active sites for propane oxidation: some generic considerations. Top Catal 54:627–638
17. Amakawa K, Kolen'ko YV, Villa A, Schuster ME, Csepei L-I, Weinberg G, Wrabetz S, Naumann d'Alnoncourt R, Girgsdies F, Prati L, Schlögl R, Trunschke A (2013) Multifunctionality of crystalline MoV(TeNb) M1 oxide catalysts in selective oxidation of propane and benzyl alcohol. ACS Catal 3:1103–1113
18. Deniau B, Nguyen TT, Delichere P, Safonova O, Millet JMM (2013) Redox state dynamics at the surface of MoVTe(Sb)NbO M1 phase in selective oxidation of light alkanes. Top Catal 56:1952–1962
19. Cheng MJ, Goddard WA (2015) In silico design of highly selective Mo-V-Te-Nb-O mixed metal oxide catalysts for ammoxidation and oxidative dehydrogenation of propane and ethane. J Am Chem Soc 137:13224–13227
20. Goddard WA, Mueller JE, Chenoweth K, van Duin ACT (2010) ReaxFF Monte Carlo reactive dynamics: application to resolving the partial occupations of the M1 phase of the MoVNbTeO catalyst. Catal Today 157:71–76
21. Melzer D, Mestl G, Wanninger K, Zhu Y, Browning ND, Sanchez-Sanchez M, Lercher JA (2019) Design and synthesis of highly active MoVTeNb-oxides for ethane oxidative dehydrogenation. Nat Commun 10:4012
22. Shinotsuka H, Tanuma S, Powell CJ, Penn DR (2015) Calculations of electron inelastic mean free paths. X. Data for 41 elemental solids over the 50 eV to 200 keV range with the relativistic full Penn algorithm. Surf Interface Anal 47:871–888
23. Heine C, Havecker M, Trunschke A, Schlögl R, Eichelbaum M (2015) The impact of steam on the electronic structure of the selective propane oxidation catalyst MoVTeNb oxide (orthorhombic M1 phase). Phys Chem Chem Phys 17:8983–8993
24. Sanchez Sanchez M, Girgsdies F, Jastak M, Kube P, Schlögl R, Trunschke A (2012) Aiding the self-assembly of supramolecular polyoxometalates under hydrothermal conditions to give precursors of complex functional oxides. Angew Chem Int Ed 51:7194–7197
25. Pyrz WD, Blom DA, Sadakane M, Kodato K, Ueda W, Vogt T, Buttrey DJ (2010) Atomic-level imaging of Mo-V-O complex

oxide phase intergrowth, grain boundaries, and defects using HAADF-STEM. Proc Natl Acad Sci 107:6152–6157
26. Kolen'ko YV, Zhang W, d'Alnoncourt RN, Girgsdies F, Hansen TW, Wolfram T, Schlögl R, Trunschke A (2011) Synthesis of MoVTeNb oxide catalysts with tunable particle dimensions. ChemCatChem 3:1597–1606
27. Concepción P, Hernández S, Nieto JML (2011) On the nature of active sites in MoVTeO and MoVTeNbO catalysts: the influence of catalyst activation temperature. Appl Catal A 391:92–101
28. Sanfiz AC, Hansen TW, Teschner D, Schnörch P, Girgsdies F, Trunschke A, Schlögl R, Looi MH, Hamid SBA (2010) Dynamics of the MoVTeNb Oxide M1 phase in propane oxidation. J Phys Chem C 114:1912–1921
29. Weber T, Muijsers JC, van Wolput JHMC, Verhagen CPJ, Niemantsverdriet JW (1996) Basic reaction steps in the sulfidation of crystalline MoO3 to MoS2, As Studied by X-ray photoelectron and infrared emission spectroscopy. J Phys Chem 100:14144–14150
30. Smith MR, Ozkan US (1993) The partial oxidation of methane to formaldehyde: role of different crystal planes of MoO3. J Catal 141:124–139
31. Hävecker M, Wrabetz S, Kröhnert J, Csepei L-I, Naumann d'Alnoncourt R, Kolen'ko YV, Girgsdies F, Schlögl R, Trunschke A (2012) Surface chemistry of phase-pure M1 MoVTeNb oxide during operation in selective oxidation of propane to acrylic acid. J Catal 285:48–60
32. Bahl MK, Watson RL, Irgolic KJ (1977) X-ray photoemission studies of tellurium and some of its compounds. J Chem Phys 66:5526–5535
33. Geyer-Lippmann J, Simon A, Stollmaier F (1984) Photoelektronenspektroskopie an Niobiodiden. Zeitschrift Für Anorganische Und Allgemeine Chemie 516:55–66
34. Teixeira da Silva VLS, Schmal M, Oyama ST (1996) Niobium carbide synthesis from niobium oxide: study of the synthesis conditions, kinetics, and solid-state transformation mechanism. J Solid State Chem 123:168–182
35. Sawatzky GA, Post D (1979) X-ray photoelectron and Auger spectroscopy study of some vanadium oxides. Phys Rev B 20:1546–1555
36. Bliznakov G, Pesheva Y, Klissurski D, Marinov M, Kozhukharov V (1987) Methanol oxidation on V2O5MoO3TeO3 catalysts. Appl Catal 29:211–218
37. Baca M, Millet J-MM (2005) Bulk oxidation state of the different cationic elements in the MoVTe(Sb)NbO catalysts for oxidation or ammoxidation of propane. Appl Catal A 279:67–77
38. Trunschke A, Noack J, Trojanov S, Girgsdies F, Lunkenbein T, Pfeifer V, Havecker M, Kube P, Sprung C, Rosowski F, Schlogl R (2017) The impact of the bulk structure on surface dynamics of complex Mo-V-based oxide catalysts. Acs Catal 7:3061–3071
39. Sadakane M, Kodato K, Yasuda N, Ishikawa S, Ueda W (2019) Thermal behavior, crystal structure, and solid-state transformation of orthorhombic Mo–V oxide under nitrogen flow or in air. ACS Omega 4:13165–13171
40. Bhore NA, Klein MT, Bischoff KB (1990) Species rank in reaction pathways: application of Delplot analysis. Chem Eng Sci 45:2109–2116
41. Bhore NA, Klein MT, Bischoff KB (1990) The delplot technique: a new method for reaction pathway analysis. Ind Eng Chem Res 29:313–316
42. Li X, Iglesia E (2008) Kinetics and mechanism of ethane oxidation to acetic acid on catalysts based on Mo−V−Nb oxides. J Phys Chem C 112:15001–15008
43. Sobolev VI, Koltunov KY (2013) Oxidative and non-oxidative degradation of C1–C3 carboxylic acids over V2O5/TiO2 and MoVTeNb oxides: a comparative study. Appl Catal A 466:45–50
44. Zhu YY, Sushko PV, Melzer D, Jensen E, Kovarik L, Ophus C, Sanchez-Sanchez M, Lercher JA, Browning ND (2017) Formation of oxygen radical sites on MoVNbTeOx by cooperative electron redistribution. J Am Chem Soc 139:12342–12345
45. Kardash TY, Lazareva EV, Svintsitskiy DA, Kovalev EP, Bondareva VM (2019) Effect of selenium additives on the physicochemical and catalytic properties of VMoTeNbO catalysts in the oxidative dehydrogenation of ethane. Kinet Catal 60:355–365
46. Zboray M, Bell AT, Iglesia E (2009) Role of C−H bond strength in the rate and selectivity of oxidative dehydrogenation of alkanes. J Phys Chem C 113:12380–12386